Isoelectric point-amyloid formation of α-synuclein extends the generality of the solubility and supersaturation-limited mechanism

Koki Furukawa [a,1], Cesar Aguirre [a,1], Masatomo So [a,1], Kenji Sasahara [a], Yohei Miyanoiri [a], Kazumasa Sakurai [b], Keiichi Yamaguchi [a], Kensuke Ikenaka [c], Hideki Mochizuki [c], Jozsef Kardos [d], Yasushi Kawata [e], Yuji Goto [a,*]

[a] Institute for Protein Research, Osaka University, Yamadaoka 3-2, Suita, Osaka, 565-0871, Japan
[b] Institute of Advanced Technology, Kindai University, Wakayama, 649-6493, Japan
[c] Department of Neurology, Graduate School of Medicine, Osaka University, Yamadaoka 2-2, Suita, Osaka, 565-0871, Japan
[d] ELTE NAP Neuroimmunology Research Group, Department of Biochemistry, Eötvös Loránd University, Pázmány P. Sétány 1/C, Budapest, 1117, Hungary
[e] Department of Chemistry and Biotechnology, Graduate School of Engineering, Tottori University, Tottori, 680-8552, Japan

ARTICLE INFO

ABSTRACT

Proteins in either a native or denatured conformation often aggregate at an isoelectric point (pI), a phenomenon known as pI precipitation. However, only a few studies have addressed the role of pI precipitation in amyloid formation, the crystal-like aggregation of denatured proteins. We found that α-synuclein, an intrinsically disordered protein of 140 amino acid residues associated with Parkinson's disease, formed amyloid fibrils at pI (= 4.7) under the low-sodium phosphate conditions. Although α-synuclein also formed amyloid fibrils at a wide pH range under high concentrations of sodium phosphate, the pI-amyloid formation was characterized by marked amyloid-specific thioflavin T fluorescence and clear fibrillar morphology, indicating highly ordered structures. Analysis by heteronuclear NMR in combination with principal component analysis suggested that amyloid formation under low and high phosphate conditions occurred by distinct mechanisms. The former was likely to be caused by the intermolecular attractive charge-charge interactions, where α-synuclein has +17 and −17 charges even with the zero net charge. On the other hand, the latter was caused by the phosphate-dependent salting-out effects. pI-amyloid formation may play a role in the membrane-dependent amyloid formation of α-synuclein, where the negatively charged membrane surface reduces the local pH to pI and the membrane hydrophobic environment enhances electrostatic interactions. The results extend the supersaturation-limited mechanism of amyloid formation: Amyloid fibrils are formed under a variety of conditions of decreased solubility of denatured proteins triggered by the breakdown of supersaturation.

1. Introduction

Amyloid fibrils, fibrillar aggregates of denatured proteins associated with amyloidoses, are formed under numerous conditions (Riek and Eisenberg, 2016; Sipe et al., 2016; Chiti and Dobson, 2017; Eisenberg and Sawaya, 2017). First, increased concentrations of amyloidogenic proteins are the most important risk factor for amyloid formation and thus the development of amyloidoses. Second, although spontaneous nucleation does not easily occur, the nucleation period is shortened by the addition of preformed fibrils, i.e. "seeds". Third, studies in vitro suggested that different additives can accelerate or suppress amyloid formation, suggesting that additives alter the solubility of amyloidogenic precursors. Fourth, mechanical acceleration of amyloid formation by ultrasonic irradiation or shaking revealed that agitation is important for triggering amyloid nucleation. Based on these observations, amyloid fibrils are crystal-like one dimensional aggregates of denatured proteins that are formed above solubility coupled with the breakdown of supersaturation (Jarrett and Lansbury Jr, 1993; Wetzel, 2006; Yoshimura et al., 2012; So et al., 2016; Adachi et al., 2018). Thus, amyloid formation is a phase transition from a solution phase to solid phase. This similarity also suggests that amorphous aggregates of denatured proteins are glass-like precipitates produced when the driving forces of aggregation are too

strong. According to the above scenario, any conditions or compounds that reduce the solubility of proteins have the potential to induce amyloid fibrils.

In addition, other factors derived from the intrinsic properties of amyloidogenic proteins seem to have an influence on amyloidogenicity. Brender et al. (2015) have reported the existence of a "micelle-like" oligomeric state in the islet amyloid polypeptide (IAPP), characterized by a critical concentration detectable by pyrene fluorescence. This research group found that IAPP variants with low amyloidogenicity had higher oligomeric critical concentration values than the native IAPP. The role of supersaturation in oligomer formation is an important issue to be addressed.

Among the many conditions leading to protein aggregation, the iso-electric point (pI) precipitation is one of the most typical properties of proteins occurring in both native and denatured states (Voet and Voet, 1995). pI precipitation is used for the purification and processing of proteins. Some types of cheese (e.g. Cottage cheese) are prepared by pI precipitation of milk caseins with a pI of 4.6. However, the role of pI precipitation in amyloid formation has not been focused on except in a few studies. Schmittschmitt and Scholtz (Schmittschmitt and Scholtz, 2003) summarized that the pH at maximal amyloid formation is near the pI value for a number of proteins, including ribonuclease Sa, and its variants, α-synuclein (αSN), transthyretin, and amyloid β peptide, suggesting that intrinsic solubility determined by the pI is an important factor for amyloid formation. Dokouhaki et al. (2017) examined the pH-dependent amyloid formation of Chaplin E by experiments and molecular dynamics simulations. Chaplin E, one of five self-assembling peptides secreted by Streptomyces coelicolor with a pI value of 6.7, exhibited rapid amyloid formation at pI or pH 10.0, suggesting a relationship between protein net charge and amyloid formation. Although the pI amyloid formation has been reported in several studies, the details, especially salt concentration dependence, are still unclear.

αSN, an intrinsically disordered protein of 140 amino acid residues and pI value of 4.7, is responsible for several synucleinopathies, including Parkinson's disease (PD), dementia with Lewy bodies (DLB), and multiple-system atrophy (MSA) (Martí et al., 2003), and forms amyloid fibrils in Lewy bodies (Araki et al., 2019). The αSN sequence can be divided into three domains: N-terminus (positively charged), NAC (hydrophobic region required for amyloid formation), and C-terminus domains (negatively charged) (Fig. 1A). We have been investigating the mechanism of amyloid formation of αSN under different conditions aided by acceleration with ultrasonic irradiation. In fact, agitation-dependent amyloid formation is a complicated reaction to which various factors contribute. Ultrasonic irradiation produces cavitation bubbles with hydrophobic air-water interfaces, at which proteins concentrate, breaking supersaturation and leading to amyloid formation (Campioni et al., 2014; Nakajima et al., 2016). Fibril surfaces induce the accumulation of protein monomers and accelerate nucleation (Yagi et al., 2014; Brender et al., 2019), referred to as secondary nucleation (Gaspar et al., 2017). Agitation also induces fibril fragmentation and increases the number of active ends, accelerating amyloid formation. On the other hand, high concentrations of salts have been assumed to decrease protein solubility and accelerated amyloid formation (Munishkina et al., 2004; Yagi et al., 2015; de Oliveira and Silva, 2019; Bousset et al., 2013).

During our studies on amyloid formation of αSN, we found by chance that αSN dissolved in deionized water easily formed amyloid fibrils upon agitation by ultrasonic irradiation, where the pH of the solution was near the pI value (= 4.7). The dependence on pH at different sodium phosphate (NaPi) concentrations suggested that the pI precipitation of αSN at low NaPi concentrations led to amyloid formation as traditional salting-out-dependent amyloid formation at high NaPi concentrations. To clarify the mechanisms responsible for amyloid formation under different NaPi concentrations, heteronuclear NMR measurements of αSN monomers were performed in combination with principal component analysis (PCA). As a result, at low phosphate concentrations at pI, αSN assumes a

compact monomeric conformation, which, with an increase in phosphate concentration, converts to an extended monomeric conformation and then oligomers. The amyloid formation at high phosphate conditions was caused by the salting-out effects, whereas that at low phosphate conditions was caused by optimizing charge-charge interactions. The pI-dependent αSN amyloid formation may play a role in amyloid formation on or in phospholipid membranes.

2. Experimental procedures

2.1. Materials and protein preparation

Recombinant human α-synuclein (αSN) was expressed in *Escherichia coli* and purified as described previously (Yagi et al., 2005, 2010). In all experiments, lyophilized αSN was dissolved in MilliQ water and filtered by Millex-GV with a pore size of 0.22 μm (Merck, Tokyo, Japan). Then, a PD-10 column (GE Healthcare Japan Co., Tokyo, Japan) was used for the removal of residual salt prior to the preparation of all monomeric samples. After the removal of salt, the concentration of αSN was measured spectrophotometrically using a molar extinction coefficient of $5120\ M^{-1}cm^{-1}$ at 280 nm. The pH of all samples was adjusted to pH 4.7 by sodium phosphate buffer with an error of less than 0.1 by pH meter LAQUA F-72 (HORIBA Ltd., Kyoto, Japan).

ThT was obtained from Wako Pure Chemical Industries, Ltd. (Osaka, Japan). All other reagents were obtained from Nacalai Tesque, Inc. (Kyoto, Japan).

2.2. Amyloid formation with microplates

The sample solutions of 200 μL containing 0.3, 0.1, or 0.03 mg/mL of αSN, 0–500 mM NaPi (pH 2–9), and 5 μM ThT were prepared in each well of a 96-well microplate at 37 °C. Five wells were used for each solution condition to confirm reproducibility. pH values of samples were confirmed by a pH meter (LAQUA F-72, HORIBA, Kyoto, Japan) before fibril formation.

ThT fluorescence was measured using the Handai Amyloid Burst Inducer (HANABI) (CORONA ELECTRIC, Ibaraki, Japan), in which a microplate reader was combined with a water bath-type ultrasonicator, with excitation and emission wavelengths at 445 and 485 nm, respectively (Umemoto et al., 2014). Ultrasonication was applied to accelerate amyloid formation with a cycle of 1-min irradiation and 9-min quiescence. The lag time was calculated as the time at which the kinetics of the ThT assay reached 1/10 of the maximum intensity.

2.3. CD and TEM measurements

Far-UV CD spectra (200–250 nm) were recorded using a J-820 spectropolarimeter (Jasco Co., Ltd., Tokyo, Japan) at 37 °C with a scan rate of 20 nm/min, a bandwidth of 1 nm, and a response time of 4 s employing a quartz cell with 1-mm path length. A buffer spectrum was subtracted and data were expressed as mean residue ellipticity, $[\theta]$.

TEM images were obtained on a Hitachi H-7650 Transmission Electron Microscope (Hitachi, Tokyo) operated at 80 kV. Samples were placed onto copper grids (400-mesh) covered with carbon-coated collodion film (Nisshin EM, Tokyo), incubated for 1 min at room temperature. The samples were negatively stained with 10 μL of a 1% (w/v) solution of phosphotungstic acid (PTA) for 5, 50 and 100 mM NaPi, or 1% (w/v) of uranyl acetate for 500 mM NaPi, then incubated for 1 min, and finally washed again with 10 μL of deionized water. The magnification working interval ranged between × 5000 and × 30 000.

2.4. Estimation of soluble and insoluble fractions

An aliquot of 200 μL of the sample solution was centrifuged at $100\ 000 \times g$ at 20 °C for 1 h. Supernatants were carefully transferred into
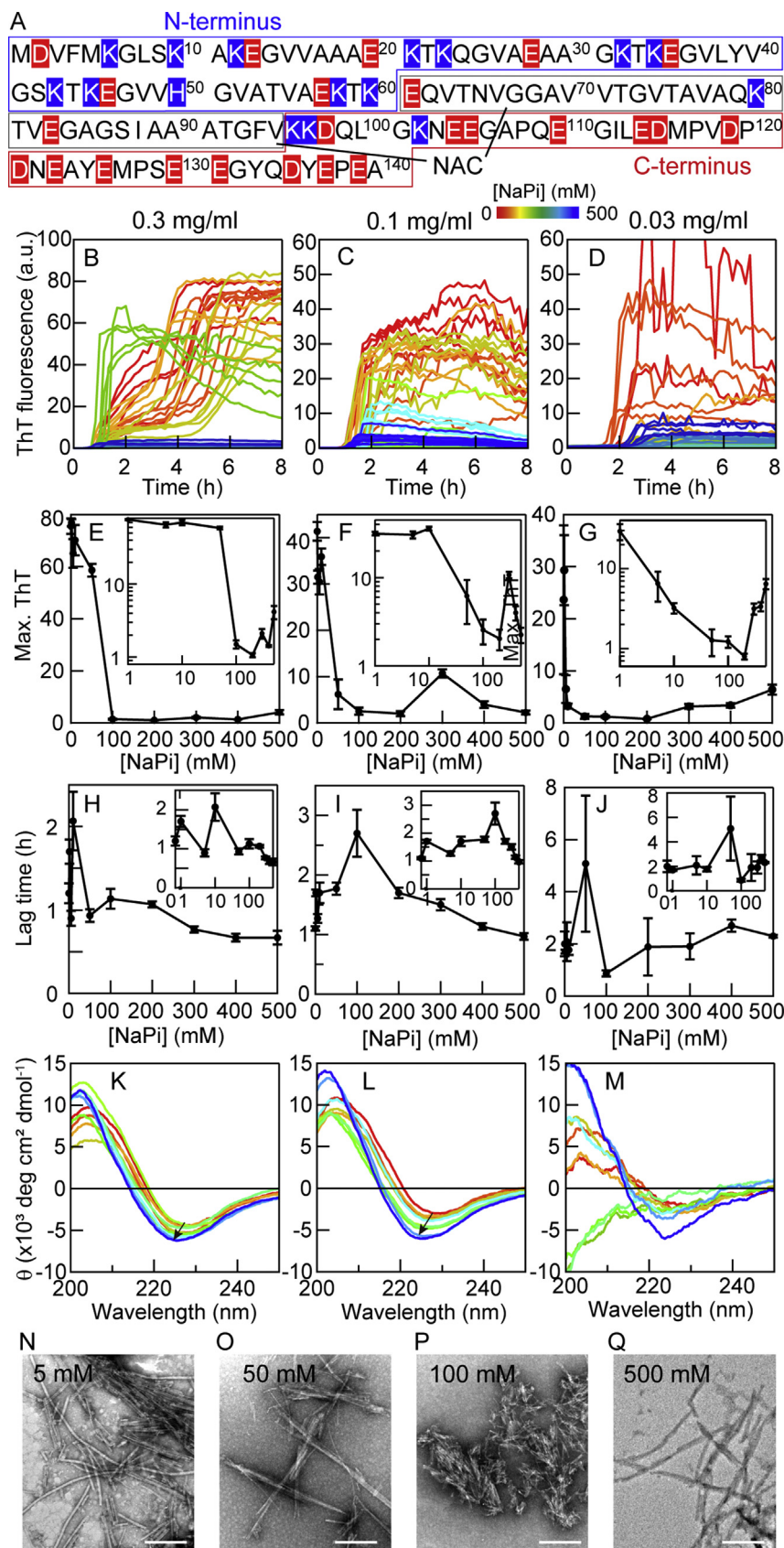
Fig. 1. Amyloid formation of αSN at pI. (A) Amino acid sequence of αSN with N-terminus (1–60 residues), NAC (61–95 residues), and C-terminus (96–140 residues) domains indicated. Acidic and basic residues are highlighted in red and blue, respectively. (B–D) Kinetics of αSN amyloid formation in the presence of different concentrations of NaPi at 0.3 (B), 0.1 (C), or 0.03 mg/mL of (D) αSN. (E–J) Dependence of the maximum ThT value (E–G) and lag time (H–J) on NaPi concentration. Insets show log plots of the same data to highlight data at low ThT values and NaPi concentrations. Data is shown as the average ± s.d. (n = 5). (K–M) CD spectra after amyloid formation. (N–Q) TEM images of fibrils of 0.1 mg/mL of αSN. Scale bars indicate 200 nm.

new tubes, and pellets were redissolved in 5 M Gnd-HCl. Pellets were incubated for 2 h at room temperature, and then centrifuged at 800 rpm. αSN species in solubilized pellets and supernatants were quantified using a Nanodrop UV device.

2.5. Solution NMR measurements

αSN solutions at 1 mg/mL uniformly labeled with ^{15}N were prepared for 2D ^{1}H–^{15}N HSQC experiments in a duplex-wall tube. As a chemical shift reference, 10 mM sodium 4,4-dimethyl-4-silapentane-1-silfonate (DSS) dissolved in D_2O was used. The spectra were recorded on a Bruker Avance-III 950 MHz spectrometer with a cryogenic probe at 37 °C. The peak assignment at pH 4.7 was achieved by 3D HN(CA)NNH measurement, which is suitable for the signal assignments of IDPs (Weisemann et al., 1993; Harbison et al., 2012), using a Bruker Avance-III 600 MHz spectrometer equipped with a cryogenic probe at 15 °C. Data were processed by NMRPipe and analyzed using Sparky. Chemical shift perturbation (CSP) was calculated as follows,

$$\Delta \delta = \sqrt{\Delta \delta_H^2 + (\Delta \delta_N/8)^2} \qquad (1)$$

where $\Delta \delta_H$ and $\Delta \delta_N$ are the chemical shift changes (in ppm) for H and N nuclei, respectively.

The DOSY experiment was performed using non-labeled αSN and the Bruker Avance-III 800 MHz spectrometer with a cryogenic probe at 15 °C. The main-chain amide proton region (6.7–7.2 ppm) was integrated and the area was plotted against the square of gradient strength (G) as follows,

$$\ln I = -D(\gamma \delta)^2 (\Delta - \delta/3)G^2 \qquad (2)$$

where D is the diffusion coefficient, I is the integrated peak intensity, and γ is the gyromagnetic ratio of a proton (2.675×10^8 rad T^{-1} s^{-1}). The diffusion time (Δ) and duration of the defocusing gradient (δ) were set to 150 ms and 2 ms, respectively. ^{1}H 1D spectra were acquired using a gradient strength of 5–98%. The hydrodynamic radius (R_h) was calculated by the Stokes-Einstein equation assuming a spherical shape.

2.6. Principal component analysis (PCA) for ^{1}H–^{15}N HSQC spectra

The chemical shift data for each spectrum were represented as a one-dimensional vector that contains the δ_H and δ_N values. As pretreatment, raw chemical shift data were normalized as follows,

$$\delta_H = \delta_{Hraw} - \delta_{Haverage} \qquad (3)$$

$$\delta_N = \frac{\delta_{Nraw} - \delta_{Naverage}}{8} \qquad (4)$$

where δ_H and δ_N are the normalized ^{1}H and ^{15}N chemical shifts of each sample containing a certain NaPi concentration, respectively. δ_{Hraw} and δ_{Nraw} are the raw chemical shifts before normalization, and $\delta_{Haverage}$ and $\delta_{Naverage}$ are the average chemical shifts of δ_{Hraw} and δ_{Nraw}, respectively, over the NaPi concentration examined. The vectors were used to build a two-dimensional matrix **X**, in which the rows are the chemical shift data from each spectrum and the columns are the variables of NaPi concentration. The matrix size was 216 [108 (number of traceable residues) × 2 (δ_H and δ_N)] × 9 (measured NaPi concentration points).

In singular value decomposition (SVD) analysis applied on the matrix **X**, three matrices, **M**, **W**, and **V**, where **M** × **W** × **V** = **X**, were given. **V** includes some uncorrelated new variables (the PCs) and **W** represents the contribution ratios for individual PCs. The SVD of chemical shift data was performed using R, a program created by R. Ihaka and R. Gentleman (University of Auckland, New Zealand).

2.7. Dynamic light scattering (DLS)

DLS measurements were performed using 1-mg/mL αSN solutions at different NaPi concentrations and room temperature. All measurements were performed 3 times by Zetasizer μV (Malvern Panalytical, England). Hydrodynamic radii and peak width values were estimated by fitting the correlation function to exponential equations assuming a spherical shape.

3. Results

3.1. NaPi concentration dependence of αSN amyloid formation at pI

We examined the dependence of αSN amyloid formation on the NaPi concentration at pH 4.7 and different αSN concentrations (0.3, 0.1, and 0.03 mg/mL) under ultrasonic irradiation with cycles of 1-min ultra-sonication and 9-min quiescence. Distinct kinetics were observed depending on the NaPi and αSN concentrations (Fig. 1). At 0.3 mg/mL αSN, ThT fluorescence increased with a short lag time of 1–2 h at all NaPi concentrations. However, the maximal ThT fluorescence intensity varied significantly depending on the NaPi concentration. At low NaPi concentrations below 50 mM, the maximal ThT intensity was high (>60 a.u. with an initial value of ~0.05 a.u.). At intermediate (100–400 mM) and high (500 mM) NaPi concentrations, they were approximately 2 and 6% of the value at 0 mM, respectively.

At lower αSN concentrations, especially at 0.03 mg/mL of αSN, the complicated dependence of the ThT intensity on NaPi concentration was marked; ThT intensities at 50–200 mM NaPi were less than 1% of the maximum, suggesting almost no fibril formation (Fig. 1F and G). Thus, the dependence of ThT intensity on NaPi concentration demonstrated a U-shaped pattern with larger ThT values at lower NaPi concentrations. The U-shaped pattern was also observed in lag time with larger values at intermediate NaPi concentrations (10–100 mM) (Fig. H-J). This suggested that, although αSN amyloid formation occurred at both low and high NaPi concentrations, it was minimal at intermediate NaPi concentrations.

We analyzed the secondary structure and morphology of ultrasonication-induced products after ThT assays by CD and TEM, respectively. At 0.3 and 0.1 mg/mL of αSN, CD spectra were typical for the cross-β structure at all NaPi concentrations, whereas, at 0.03 mg/mL of αSN, CD spectra at intermediate NaPi concentrations were those of the disordered conformation, supporting no amyloid formation as suggested by ThT assays (Fig. 1K–M). Of note, at 0.3 and 0.1 mg/mL of αSN, the CD minima shifted from 228 nm to 225 nm with an increase in the concentration of NaPi, suggesting that the fibrils formed at low and high NaPi concentrations were distinct. TEM images of fibrils obtained by HANABI showed short frills due to the strong ultrasonication of HANABI system (Fig. S1). TEM images of fibrils obtained employing F4500 fluorimeter equipped with a weak ultrasonicator revealed typical amyloid fibrils at all NaPi concentrations, although meanwhile short fibrils dominated at intermediate NaPi concentrations (100 mM) (Fig. 1N–Q, Fig. S1).

We further estimated soluble and insoluble fractions of αSN after ThT assays at 0.1 mg/mL αSN (Fig. S2). The soluble fraction was dominated at 50 and 100 mM NaPi, whereas the insoluble fraction was dominated at other concentrations. These results suggested that at all αSN concentrations, typical rigid and long fibrils were formed.

3.2. pH-dependence of amyloid formation and phase diagrams for conformational states

To clarify the low NaPi-dependent amyloid formation, which has not been reported thus far, we examined the pH dependence of amyloid formation at 0.1 mg/mL of αSN at 5, 100, or 500 mM NaPi (Fig. 2 and Fig. S3). At 5 mM NaPi, we observed a sharp peak in the ThT fluorescence intensity at approximately pH 5.0, which was consistent with the pI value (= 4.7) of αSN, demonstrating that the fibril formation at low NaPi at pH
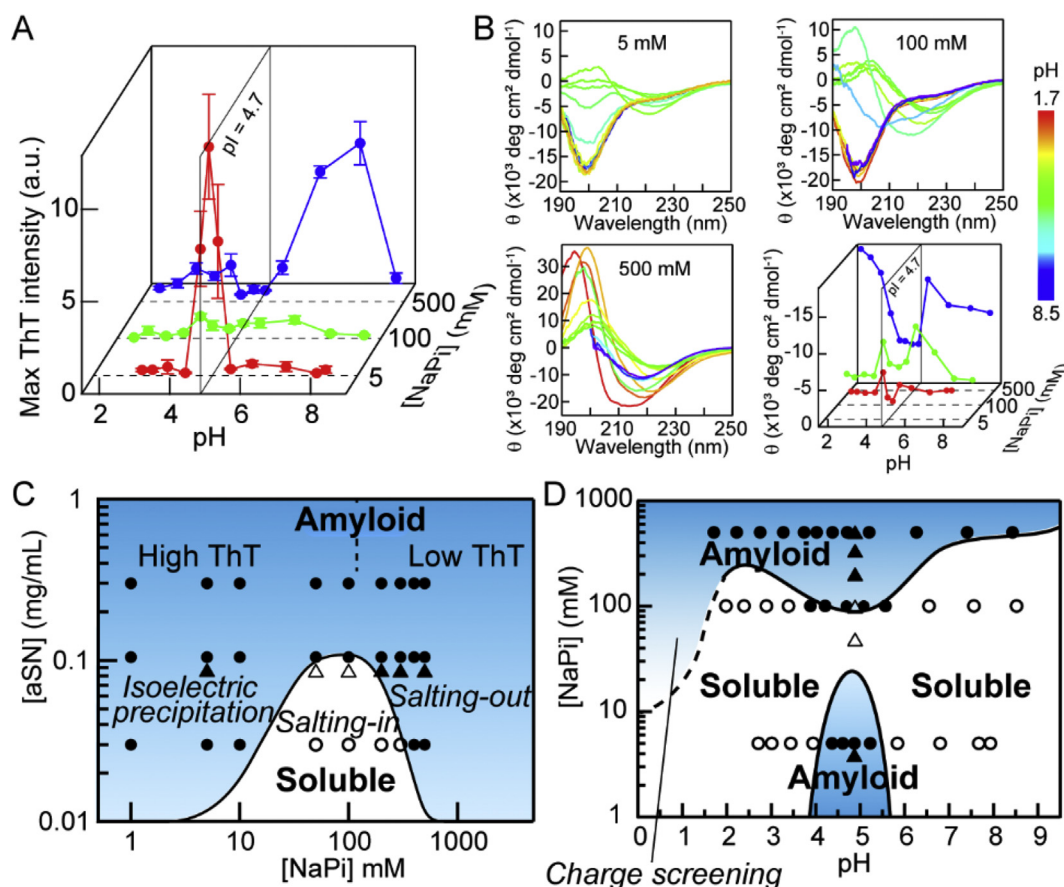
Fig. 2. pH-dependent amyloid formation of αSN at different NaPi concentrations and conformational phase diagrams. (A) Maximum ThT values at different pH and NaPi concentrations. Data is shown as the average ± s.d. (n = 5). Kinetic data are shown in Fig. S3. (B) CD spectra and the intensities at 220 nm. Different colors in CD spectra indicate different pH as defined by a color scale bar. (C) Conformational phase diagram at pI (=4.7) dependent on the concentrations of NaPi and αSN. (D) Conformational phase diagram at 0.1 mg/mL αSN dependent on pH and NaPi concentration. Data points obtained from CD (circle) and soluble and insoluble fraction measurements (triangle) were also plotted.

4.7 was indeed caused by the pI precipitation (Fig. 2A). At 100 mM NaPi, ThT fluorescence exhibited a broad maximum at pH 3–7. At 500 mM NaPi, a maximum in ThT fluorescence was observed at neutral pH regions.

According to CD spectra, at 5 mM NaPi, amyloid fibrils were formed at a narrow pH region near pI (i.e., pH 4.5–5.5), consistent with the profile of ThT fluorescence (Fig. 2B). At 100 mM NaPi, the CD spectra demonstrated amyloid formation at pH 4–6, a wider pH range than that at 5 mM NaPi. At 500 mM NaPi, the CD spectra indicated the β-sheet structure for all the samples examined, although the spectra at pH 5 with lower intensities at around 220 nm were distinct from those at acidic or neutral pH with larger intensities. Importantly, at 100 mM NaPi, a considerable amount of soluble species remained compared with those at high and low salt concentrations (Fig. S2). Thus, at 100 mM NaPi, more complicated reactions such as the formation of protofibrils, oligomers, or amorphous aggregates might occur and the details need to be investigated further. At 500 mM NaPi, amyloid fibrils prevailed at all pH regions examined, although the distinct ThT fluorescence and CD properties suggested that the amyloid conformation depended on pH.

Taking these results together, we constructed phase diagrams of αSN conformational states depending on αSN and NaPi concentrations at pH 4.7 (Fig. 2C), and on NaPi concentration and pH (Fig. 2D). As for the αSN- and NaPi-dependent phase diagram, it was clear that separate amyloid regions at the low αSN concentration merged at high αSN concentrations because higher protein concentrations extended the two amyloid regions. As for the NaPi- and pH-dependent phase diagram, the pI-dependent amyloid formation was evident only at low NaPi concentrations, and at

high NaPi concentrations, the amyloid region prevailed over a wider pH range probably due to the salting-out mechanism. The phase diagrams suggested that the complicated dependence of amyloid formation on NaPi concentration or pH can be explained in terms of the combined effects of two types of mechanisms, pI-dependent and salting-out-dependent amyloid formation.

3.3. Conformation of αSN at pI in the presence of different concentrations of NaPi

In order to characterize the monomeric state of αSN at various NaPi concentrations at pI (= 4.7), NMR spectra of αSN before aggregation were recorded in the presence of different concentrations of NaPi (Fig. 3). Without ultrasonication, αSN remained soluble during the periods of NMR measurement (~2 h). Signal assignments of 77% of the amino acid residues of αSN were achieved (Fig. 3A). When ^{1}H–^{15}N HSQC spectra of all samples were compared, curved peak shifts were observed for 91 out of 108 traceable residues (Fig. 3B and C).

To determine the number of conformational states of soluble αSN at different NaPi concentrations, principal component analysis (PCA) of HSQC chemical shift data was performed. PCA is a multivariate analysis used to simplify the complexity in high-dimensional data by geometrically projecting data onto lower dimensions called principal components (PCs) (Lever et al., 2017). PCA can remove the contribution of noise to experimental data and estimate the number of meaningful components such as the number of binding sites or the number of conformations (Jaumot et al., 2004; Sakurai and Goto, 2007).
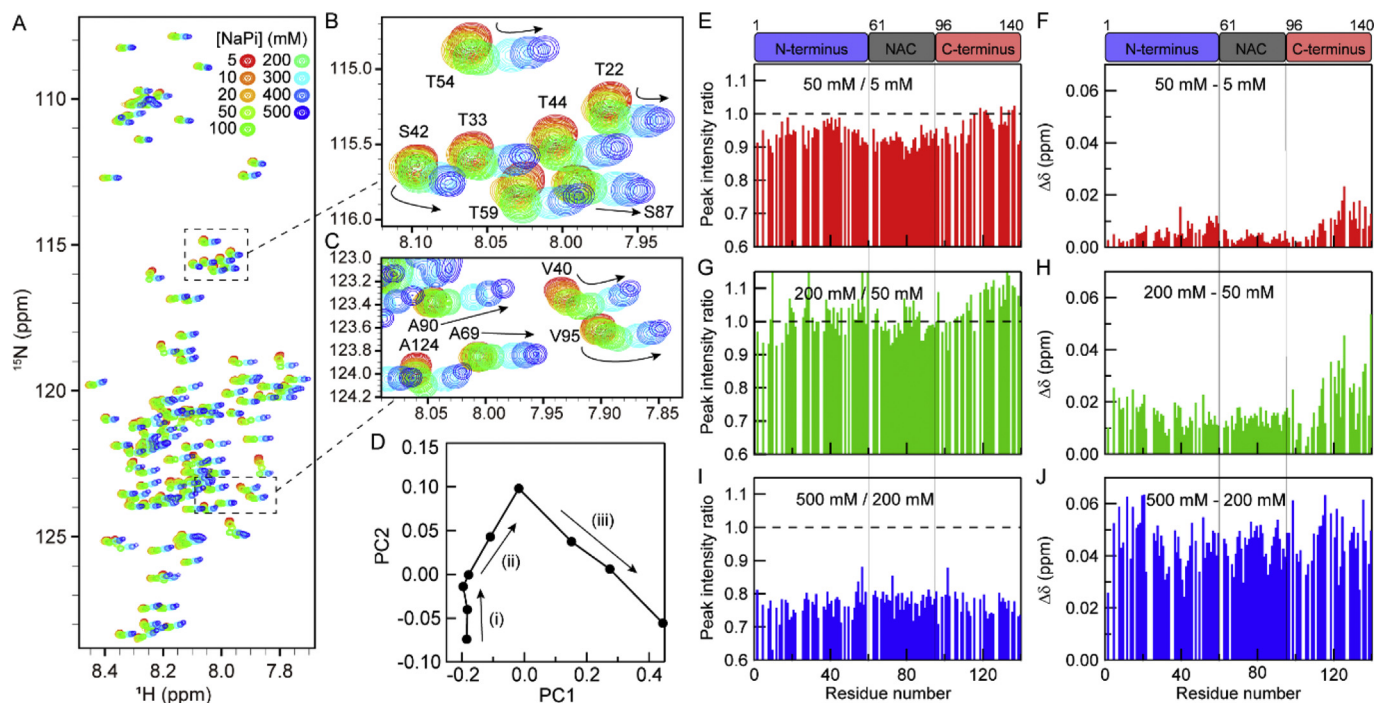
Fig. 3. Dependence of NMR spectra at different concentrations of NaPi at pI and principal component analysis of the NMR data against NaPi concentration. (A–C) ^{1}H–^{15}N HSQC spectra at different NaPi concentrations were overlaid in different colors. Arrows indicate the direction of peak movement. (D) The change in principal components 1 and 2 depending on the NaPi concentration. The numbers indicate 3 principal conformational states of αSN. (E–J) Profiles of the peak intensity and chemical shift changes in three concentration regions. (E, G, I) The peak intensity changes between 5 and 50 mM (E), 50 and 200 mM (G), and 200 and 500 mM NaPi (I). (F, H, J) The chemical shift changes between 5 and 50 mM (F), 50 and 200 mM (H), and 200 and 500 mM (J). Domains of αSN are shown on top.
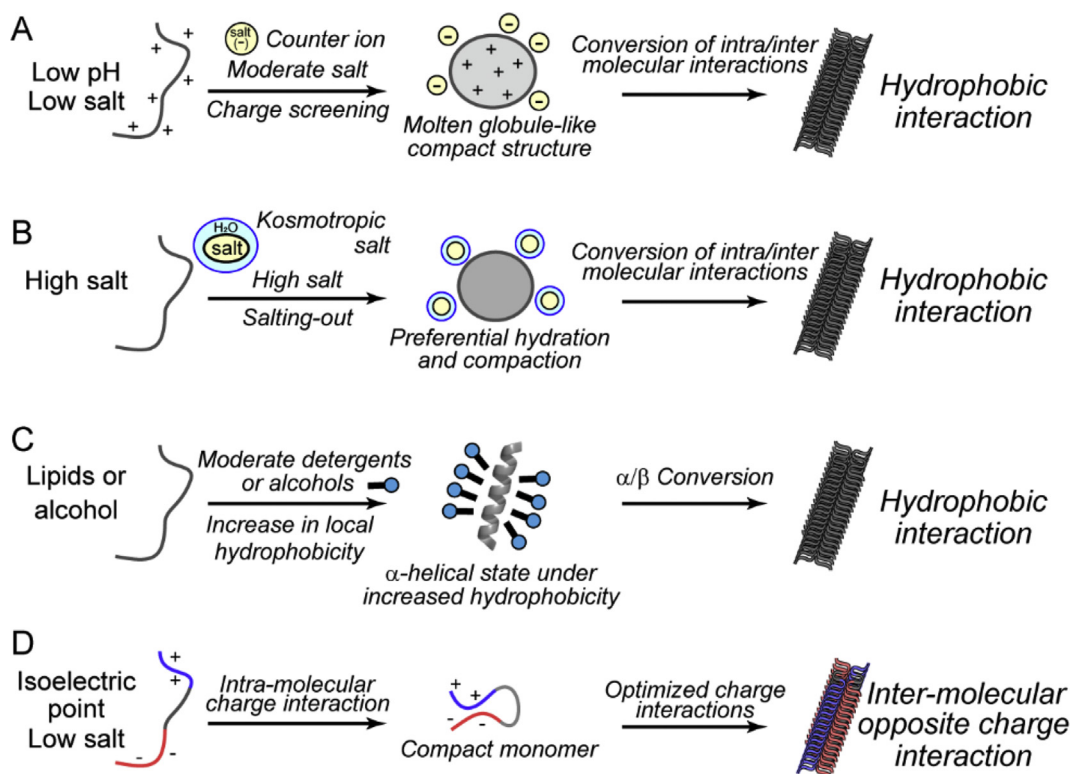

Fig. 4. Distinct mechanisms of amyloid formation based on solubility and supersaturation. (A) Counter ion-binding mechanism observed under acidic conditions in the presence of moderate concentrations of salts. (B) Salting-out mechanism observed under high salt conditions independent of pH. (C) Hydrophobic additive-binding mechanism observed in the presence of moderate concentrations of alcohols or detergents like SDS. (D) pI-precipitation mechanism. The hydrophobic additive-binding mechanism is similar to the salting-out-dependent mechanism in that additives without charges strengthen the hydrophobic interactions, leading to the decrease in solubility and thus to amyloid formation.

As a result of the singular value decomposition of the normalized chemical shift data by R statistical software, we obtained 9 PCs and corresponding contribution ratios (Fig. S4A). The cumulative contribution ratio of the PC1 was 0.75 and that of the first 2 PCs was 0.92. The plot of PCs against the NaPi concentration revealed that PC1 and PC2 changed smoothly against the NaPi concentration, whereas PC3 was low in intensity over the NaPi concentrations examined (Fig. S4B). Thus, the two dominant PCs were sufficient to describe most of the observed signal movements. The plot of PC2 against PC1 demonstrated three directions of chemical shift changes (Fig. 3D), suggesting that there are 3 principal conformational states of αSN depending on the NaPi concentration.

We focused on the four different NaPi concentrations, and obtained the stepwise differences among them in terms of NMR signal intensities and chemical shift changes (Fig. 4): (i) 5–50 mM at which PC1 was constant and PC2 decreased, (ii) 50–200 mM at which both PC1 and PC2 increased, and (iii) 200–500 mM at which PC1 increased, but PC2 decreased (Fig. S4B, Fig. 3D). In order to compare chemical shift movements, we calculated chemical shift perturbation (CSP).

When the NaPi concentration was increased from 5 to 50 mM, the intensities for N- and C-terminal residues remained almost unchanged, whereas those of the NAC region slightly decreased, suggesting that intermolecular hydrophobic interactions between NAC regions increased with increasing NaPi concentration (Fig. 3E). The chemical shifts were larger for residues in the N- and C-terminals than those in the NAC region, suggesting that the interactions between these 2 domains changed due to the change in NaPi concentration (Fig. 3F).

From 50 to 200 mM NaPi, no significant change in peak intensity was observed (Fig. 3G). Note that the intensities at K10, A29, E57, K60, and D115 may be incorrect because of significant overlapping of peaks. In contrast, the CSP of the C-terminus was relatively high, suggesting that its mobility increased with an increase in NaPi concentration (Fig. 3H).

From 200 to 500 mM NaPi, a significant decrease in the NMR peak was observed over the entire sequence, suggesting that oligomers or other aggregates were formed (Fig. 3I). As the CSP had no significant difference, no information about structural change was obtained (Fig. 3J).

3.4. Hydrodynamic radii of αSN at pI in the presence of different concentrations of NaPi

At pI, the N- and C-termini of αSN are mainly positively and negatively charged, respectively (Fig. 1A). These regions are capable of interacting with each other and thus affect the structure depending on the NaPi concentration. In order to obtain additional information about soluble αSN conformations at pI, we measured the hydrodynamic radius (R_h) of αSN at different concentrations of NaPi by NMR and dynamic light scattering (DLS). The Rh values at pH 4.7 estimated by DLS were 2.4, 3.2, 3.2, and 3.9 nm at 0, 50, 100, and 500 mM NaPi, respectively (Fig. S5; Table S1). The R_h value at pH 7.4 in the presence of 100 mM NaCl and 20 mM NaPi was reported to be 3.4 nm, representing an extended monomeric structure (Morar et al., 2001; Uversky et al., 2001a,b). The R_h value observed by DLS measurements was 3.2 nm at 50 or 100 mM NaPi at pH 4.7, suggesting that αSN monomers formed extended structures as observed at pH 7.4. On the other hand, αSN formed a compact structure with the R_h value of 2.4 nm at low NaPi concentrations at pH 4.7. At 500 mM NaPi, the R_h value was 3.9 nm and the distribution profile was broadened, suggesting a population of oligomeric molecules.

We also performed DOSY measurements (Tanner, 1970) in the presence of 5, 50, or 200 mM NaPi at pH 4.7, and the R_h values were 2.9, 3.2, and 3.5 nm, respectively. The R_h value obtained by DOSY measurement at pH 7.0 in the presence of 20 mM NaPi was 3.4 nm. All values were consistent with those measured by DLS (Table S1). Taken together, αSN at pI with low NaPi concentrations formed a compact structure, whereas an extended conformation was dominant at intermediate NaPi concentrations. At 500 mM NaPi, a population of oligomers may be involved.

The R_h value of αSN measured without NaPi at pI (2.4 nm), which was lower than that at pH 7.0 (3.4 nm), corresponds to that reported previously (2.66 nm) (Morar et al., 2001) and that calculated by restraining molecular dynamics simulation (2.72 nm) (Dedmon et al., 2005). Although our experiments were performed under non-crowded conditions, the R_h of αSN without NaPi at pI was close to that under crowded conditions in 1.0 M glucose (2.25 nm) (Morar et al., 2001). Therefore, αSN formed a compact conformation under low salt conditions at pI. Although the net charge is zero, it is likely that a positively charged N-terminal region and a negatively charged C-terminal region interact to form a compact structure. The R_h value of the fully unfolded model of αSN was 3.45 nm (Dedmon et al., 2005), similar to that in the presence of 100 mM NaPi at pI (3.2 nm), reflecting the major presence of extended monomers under these conditions.

4. Discussion

4.1. Amyloid formation of αSN at pI

αSN, an intrinsically disordered protein with a pI value of 4.7, has been considered to be a highly soluble protein. The purification of αSN is often performed by heating *E. coli* extracts up to 85 °C, by which other proteins are mostly removed by heat-induced precipitation. Although amyloid formation of αSN has been extensively studied, it usually requires high concentrations of salts (Munishkina et al., 2004; Yagi et al., 2015; Giehm and Otzen, 2010) or high αSN concentrations (de Oliveira and Silva, 2019; Bousset et al., 2013) and a long incubation period even under agitation or in the presence of phospholipid membranes (Terakawa et al., 2018; Ugalde et al., 2019). We unexpectedly found that αSN at relatively low concentrations (i.e., 0.03–0.3 mg/mL) forms amyloid fibrils when deionized water was used for dissolution and the resultant solution at a pH of approximately 5.0 without salt was incubated under ultrasonic agitation. The subsequent controlled sample preparation with the NaPi buffer at pH 4.7 demonstrated that amyloid fibrils were formed at NaPi concentrations below 20 mM, opposite to the traditional salt-induced amyloid nucleation. Moreover, the pH dependence under low phosphate conditions exhibited a clear peak at pH 4.7, confirming the pI-amyloid formation. αSN also formed amyloid fibrils under high salt conditions (i.e., 500 mM NaPi) at all pH ranges examined (Fig. 2), which was explained in terms of salting-out effects. Although the amyloid formation of αSN at low NaPi concentrations was unexpected, it can be simply explained by the pI precipitation.

pI precipitation occurs in the absence of intermolecular charge-charge repulsion driven mainly by intermolecular hydrophobic interactions. Although the net charge is zero at pI, it is likely that oppositely charged groups coexist, which may form salt bridges stabilizing a unique monomeric conformation. Indeed, αSN has 17 positive (15 Lys, 1 His, and 1 N-terminus) and 25 negative (6 Asp, 18 Glu, and 1 C-terminus) titratable groups (Fig. 1A). Assuming the pKa values of 10.0 for Lys, 6.0 for His, 7.0 for N-terminus, 4.1 for Asp, 4.5 for Glu, and 3.8 for C-terminus (Bjellqvist et al., 1994), the pI value was estimated to be 4.7, where large and equal numbers of positive (+17 in total from 15 Lys, 1 His, and 1 N-terminus) and negative (−17 in total form 4.8 Asp, 11.2 Glu, and 1 C-terminus) charges exist (Fig. S6). Thus, pI precipitation may be further promoted under low salt conditions where attractive charge-charge interactions can be strengthened. It is possible that additional intermolecular electrostatic attractions, including hydrogen bonds, can be formed. Thus, reducing the salt concentration is expected to be a useful approach for pI precipitation.

4.2. Molecular mechanism of pI-amyloid formation

The NMR analysis of soluble αSN suggested the mechanism of amyloid formation at pI under low salt-conditions. The N- and C-termini of αSN have charged groups with net positive and negative charges, respectively. The changes in chemical shifts and R_h values upon increasing the NaPi concentration from 5 to 50 mM suggested that αSN under low salt

conditions assumed a compact conformation in which the N- and C-terminal regions interact electrostatically. The increase in NaPi concentration from 5 to 50 mM also caused the decreases in NMR peak intensities of the NAC region, suggesting the exposure of the NAC region upon release of the N- and C-terminal interaction. This situation of the NAC region being shielded from exposure to the solution by taking a compact conformation has been reported in mammalian cells (Theillet et al., 2016). Thus, it is likely that the pI-amyloid formation is caused by the strengthened intermolecular electrostatic interactions under low salt conditions with the intramolecular interactions remaining similar (Fig. 4D).

Thus far, several types of αSN amyloid structures have been reported using cryo-electron microscopy helical reconstruction methodologies (Li et al., 2018) (Fig. S7). In these structures, each molecule in the protofilaments features a Greek key-like topology (Li et al., 2018) (or a kernel structure of a bent β-arch (Li et al., 2018)). Monomers accumulate in a staggered manner to form cross-β structures. Two protofilaments associate at the hydrophobic central regions to form a polar fibril, exposing both N- and C-terminal regions to solvents. However, detailed topologies and structures revealed significant polymorphs, suggesting their potential role in distinct pathogenesis.

When the atomic structures of monomers in protofilaments were inspected, N-terminal and C-terminal regions both exposed to solvent were relatively close to each other, likely satisfying the attractive charge-charge interactions. In the fibrils, although the same charges are aligned in a staggered manner, the counter ions present in solution may neutralize the charge repulsion. Moreover, aligned positive and negative charges may interact electrostatically, stabilizing the polar fibrils. In the latter case, amyloid fibrils are further stabilized under low salt conditions at pI.

Although the exact mechanism of amyloid formation at pI is far from clear, it might be possible that the replacement of the intramolecular charge-charge attractions by the intermolecular interactions contributes to the pI-amyloid formation leading to domain swapping-type aggregates (Liu and Eisenberg, 2002; Nelson and Eisenberg, 2006). However, the role of domain swapping in amyloid formation is not clear (Li et al., 2011; Žerovnik et al., 2011).

4.3. Different conditions to form amyloid fibrils

Thus far, several solvent conditions have been reported to reduce the solubility of proteins and peptides, and thus to induce amyloid fibrils (Fig. 4). First, moderate anion conditions under acidic pH shield electrostatic repulsion between positively charged groups by anion binding, revealing intrinsic hydrophobic interactions, thereby leading to amyloid formation (Yoshimura et al., 2012; Raman et al., 2005) (Fig. 4A). These conditions often stabilize the acidic molten globule states (Goto et al., 2018). Even at neutral pH, metal cation has also been proposed to interact with negatively charged C-terminus of αSN, masking the charge repulsion and thus resulting in the promotion of amyloid formation, similar to charge screening effects (Uversky et al., 2001c). Second, high salt conditions often at neutral pH cause amyloid formation by salting-out effects (Munishkina et al., 2004; Yagi et al., 2015) (Fig. 4B). In addition, phosphate ions can affect both water-water and protein water interaction, leading to acceleration of fibril formation and stabilization of amyloid fibrils (Munishkina et al., 2004; de Oliveira et al., 2016). Third, moderate concentrations of detergents (e.g. SDS) or alcohols (e.g. 2,2,2-trifluoroethanol or 3,3,3,3′,3′,3′-hexafluoro-2-propanol) strengthen hydrophobic interactions between proteins thorough interactions with hydrophobic groups of amphiphilic detergents or alcohols (Yamaguchi et al., 2006; Otzen, 2010; So et al., 2015) (Fig. 4C). These hydrophobic additives cause amyloid formation by strengthening hydrophobic interactions before complete dissolution of the proteins at high concentrations of additives (Yamaguchi et al., 2006; Otzen, 2010). Here, we add the fourth condition of amyloid formation of reducing the salt concentration at pI (Fig. 4D). By reducing the salt concentration, we can maximize the opposite charge-charge attractions, leading to intermolecular charge-charge interactions and thus amyloid formation.

αSN has been reported to interact with negatively charged phospholipid membranes dominantly by the N-terminal and NAC regions with negatively charged C-terminal regions exposed to solvent (Terakawa et al., 2018; Fusco et al., 2014). Binding to the hydrophobic interior of membranes through the N-terminal and NAC domains has been assumed to accelerate amyloid nucleation and increase the local concentration of αSN. When the pI-amyloid formation of αSN was compared with the membrane-dependent amyloid formation, the environment with lower polarity (or decreased dielectric constant) was the same. In addition and most importantly, it has been assumed that the local pH in the vicinity of negatively charged phospholipids is lower by up to 2-fold than the bulk pH because the negatively charged polar heads give rise to an electrical surface potential, which in turn reduces the surface pH (van der Goot et al., 1991). The local decrease in pH was assumed to denature the native conformation of proteins, inducing acidic molten globule states and their interaction with or insertion into membranes (van der Goot et al., 1991; Bychkova et al., 1996). We assume that the pI-dependent mechanism plays a role in the phospholipid membrane-dependent amyloid formation of αSN. Recently, it has been suggested that plasma membranes can be disrupted by amyloidogenic peptides, such as Aβ and IAPP, through a two-step mechanism which involves pore formation and lipid extraction from the bilayer mediated by lipid-fibril interactions (Sciacca et al., 2018). In this scenario, a gradient of pH in the vicinity of the membranes would favor not only the formation of amyloid fibrils by the proposed pI-dependent mechanism, but also the interaction between fibrils and the extracted lipids probably by increasing hydrophobic lipid-fibril interactions. Whether the pI-amyloid formation plays a role in the membrane-assisted amyloid formation of αSN is of interest. If this is the case, the atomic structure of pI-induced amyloid fibrils may be different from those reported thus far (Fig. S5), especially regarding the role of the charged N- and C-terminal interactions.

Among the four conditions, the anion binding mechanism under acidic pH (Fig. 4A) was not clear for αSN (Fig. 2D). Munishkina et al. (2004) compared amyloid formation of αSN at neutral pH and low pH, suggesting that, although the salting-out effects dominated at neutral pH, counter anion binding plays a role in amyloid formation at acidic pH. Although it is unclear why the anion binding mechanism was not observed at acidic pH (Fig. 2), it is possible that the effects of phosphate as counter ions to bind to the positive charges are not strong even at pH 2.

5. Conclusions

We confirmed that αSN, a typical intrinsically disordered amyloidogenic protein, forms amyloid fibrils at pI under low salt conditions. Taken together, there are four distinct mechanisms of amyloid formation (Fig. 4). Considering the complicated mechanism of αSN amyloid formation (de Oliveira and Silva, 2019), the detailed kinetics and intermediates of pI-dependent amyloid formation are far from clear. Nevertheless, our unexpected finding brought further insights into the physicochemical mechanism of amyloid formation. Moreover, we suggest that the pI-dependent mechanism plays a role in the phospholipid membrane-dependent amyloid formation of αSN. In conclusion, our study expands the general mechanism of amyloid formation in that they are crystal-like aggregates of denatured proteins formed when the concentration is higher than the solubility coupled with the breakdown of supersaturation.

Author contributions

Declaration of Competing Interest

The authors declare that they have no conflicts of interest with the contents of this article.

Acknowledgements

Appendix A. Supplementary data

Supplementary data to this article can be found online at https ://doi.org/10.1016/j.crstbi.2020.03.001.

References

Adachi, M., Noji, M., So, M., Sasahara, K., Kardos, J., Naiki, H., Goto, Y., 2018. Aggregation-phase diagrams of β_2-microglobulin reveal temperature and salt effects on competitive formation of amyloids versus amorphous aggregates. J. Biol. Chem. 293, 14775–14785.

Araki, K., Yagi, N., Aoyama, K., Choong, C.-J., Hayakawa, H., Fujimura, H., Nagai, Y., Goto, Y., Mochizuki, H., 2019. Parkinson's disease is a type of amyloidosis featuring accumulation of amyloid fibrils of α-synuclein. Proc. Natl. Acad. Sci. U.S.A. 201906124. https://doi.org/10.1073/pnas.1906124116.

Bjellqvist, B., Basse, B., Olsen, E., Celis, J.E., 1994. Reference points for comparisons of two-dimensional maps of proteins from different human cell types defined in a pH scale where isoelectric points correlate with polypeptide compositions. Electrophoresis 15, 529–539.

Bousset, L., Pieri, L., Ruiz-Arlandis, G., Gath, J., Jensen, P.H., Habenstein, B., Madiona, K., Olieric, V., Böckmann, A., Meier, B.H., et al., 2013. Structural and functional characterization of two alpha-synuclein strains. Nat. Commun. 4, 2575.

Brender, J.R., Krishnamoorthy, J., Sciacca, M.F.M., Vivekanandan, S., D'Urso, L., Chen, J., La Rosa, C., Ramamoorthy, A., 2015. Probing the sources of the apparent irreproducibility of amyloid formation: drastic changes in kinetics and a switch in mechanism due to micellelike oligomer formation at critical concentrations of IAPP. J. Phys. Chem. B 119, 2886–2896.

Brender, J.R., Ghosh, A., Kotler, S.A., Krishnamoorthy, J., Bera, S., Morris, V., Sil, T.B., Garai, K., Reif, B., Bhunia, A., et al., 2019. Probing transient non-native states in amyloid beta fiber elongation by NMR. Chem. Commun. 55, 4483–4486.

Bychkova, V.E., Dujsekina, A.E., Klenin, S.I., Tiktopulo, E.I., Uversky, V.N., Ptitsyn, O.B., 1996. Molten globule-like state of cytochrome c under conditions simulating those near the membrane surface. Biochemistry 35, 6058–6063.

Campioni, S., Carret, G., Jordens, S., Nicoud, L., Mezzenga, R., Riek, R., 2014. The presence of an air-water interface affects formation and elongation of alpha-synuclein fibrils. J. Am. Chem. Soc. https://doi.org/10.1021/ja412105t.

Chiti, F., Dobson, C.M., 2017. Protein misfolding, amyloid formation, and human disease: a summary of progress over the last decade. Annu. Rev. Biochem. 86, 27–68.

de Oliveira, G.A.P., Silva, J.L., 2019. Alpha-synuclein stepwise aggregation reveals features of an early onset mutation in Parkinson's disease. Commun. Biol. 2, 374-374.

de Oliveira, G.A.P., Marques, MdA., Cruzeiro-Silva, C., Cordeiro, Y., Schuabb, C., Moraes, A.H., Winter, R., Oschkinat, H., Foguel, D., Freitas, M.S., et al., 2016. Structural basis for the dissociation of α-synuclein fibrils triggered by pressure perturbation of the hydrophobic core. Sci. Rep. 6, 37990.

Dedmon, M.M., Lindorff-Larsen, K., Christodoulou, J., Vendruscolo, M., Dobson, C.M., 2005. Mapping long-range interactions in α-synuclein using spin-label NMR and ensemble molecular dynamics simulations. J. Am. Chem. Soc. 127, 476–477.

Dokouhaki, M., Hung, A., Day, L., Gras, S.L., 2017. The pH-dependent assembly of Chaplin E from Streptomyces coelicolor. J. Strucut. Biol. 198, 82–91.

Eisenberg, D.S., Sawaya, M.R., 2017. Structural studies of amyloid proteins at the molecular level. Annu. Rev. Biochem. 86, 69–95.

Fusco, G., De Simone, A., Gopinath, T., Vostrikov, V., Vendruscolo, M., Dobson, C.M., Veglia, G., 2014. Direct observation of the three regions in α-synuclein that determine its membrane-bound behaviour. Nat. Commun. 5, 3827.

Gaspar, R., Meisl, G., Buell, A.K., Young, L., Kaminski, C.F., Knowles, T.P.J., Sparr, E., Linse, S., 2017. Secondary nucleation of monomers on fibril surface dominates α-synuclein aggregation and provides autocatalytic amyloid amplification. Q. Rev. Biophys. 50, e6.

Giehm, L., Otzen, D.E., 2010. Strategies to increase the reproducibility of protein fibrillization in plate reader assays. Anal. Biochem. 400, 270–281.

Goto, Y., Adachi, M., Muta, H., So, M., 2018. Salt-induced formations of partially folded intermediates and amyloid fibrils suggests a common underlying mechanism. Biophys. Rev. 10, 493–502.

Harbison, N.W., Bhattacharya, S., Eliezer, D., 2012. Assigning backbone NMR resonances for full length tau isoforms: efficient compromise between manual assignments and reduced dimensionality. PloS One 7, e34679.

Jarrett, J.T., Lansbury Jr., P.T., 1993. Seeding "one-dimensional crystallization" of amyloid: a pathogenic mechanism in Alzheimer's disease and scrapie? Cell 73, 1055–1058.

Jaumot, J., Vives, M., Gargallo, R., 2004. Application of multivariate resolution methods to the study of biochemical and biophysical processes. Anal. Biochem. 327, 1–13.

Lever, J., Krzywinski, M., Altman, N., 2017. Principal component analysis. Nat. Methods 14, 641.

Li, J., Hoop, C.L., Kodali, R., Sivanandam, V.N., van der Wel, P.C.A., 2011. Amyloid-like fibrils from a domain-swapping protein feature a parallel, in-register conformation without native-like interactions. J. Biol. Chem. 286, 28988–28995.

Li, Y., Zhao, C., Luo, F., Liu, Z., Gui, X., Luo, Z., Zhang, X., Li, D., Liu, C., Li, X., 2018. Amyloid fibril structure of α-synuclein determined by cryo-electron microscopy. Cell Res. 28, 897–903.

Liu, Y., Eisenberg, D., 2002. 3D domain swapping: as domains continue to swap. Protein Sci. 11, 1285–1299.

Martí, M.J., Tolosa, E., Campdelacreu, J., 2003. Clinical overview of the synucleinopathies. Mov. Disord. 18, 21–27.

Morar, A.S., Olteanu, A., Young, G.B., Pielak, G.J., 2001. Solvent-induced collapse of α-synuclein and acid-denatured cytochrome c. Protein Sci. 10, 2195–2199.

Munishkina, L.A., Henriques, J., Uversky, V.N., Fink, A.L., 2004. Role of protein–water interactions and electrostatics in α-synuclein fibril formation. Biochemistry 43, 3289–3300.

Nakajima, K., Ogi, H., Adachi, K., Noi, K., Hirao, M., Yagi, H., Goto, Y., 2016. Nucleus factory on cavitation bubble for amyloid β fibril. Sci. Rep. 6, 22015.

Nelson, R., Eisenberg, D., 2006. Recent atomic models of amyloid fibril structure. Curr. Opin. Struct. Biol. 16, 260–265.

Otzen, D.E., 2010. Amyloid Formation in surfactants and alcohols: membrane mimetics or structural switchers? Curr. Protein Pept. Sci. 11, 355–371.

Raman, B., Chatani, E., Kihara, M., Ban, T., Sakai, M., Hasegawa, K., Naiki, H., Rao, C.M., Goto, Y., 2005. Critical balance of electrostatic and hydrophobic interactions is required for β_2-microglobulin amyloid fibril growth and stability. Biochemistry 44, 1288–1299.

Riek, R., Eisenberg, D.S., 2016. The activities of amyloids from a structural perspective. Nature 539, 227.

Sakurai, K., Goto, Y., 2007. Principal component analysis of the pH-dependent conformational transitions of bovine β-lactoglobulin monitored by heteronuclear NMR. Proc. Natl. Acad. Sci. U.S.A. 104, 15346–15351.

Schmittschmitt, J.P., Scholtz, J.M., 2003. The role of protein stability, solubility, and net charge in amyloid fibril formation. Protein Sci. 12, 2374–2378.

Sciacca, M.F.M., Tempra, C., Scollo, F., Milardi, D., La Rosa, C., 2018. Amyloid growth and membrane damage: current themes and emerging perspectives from theory and experiments on Aβ and hIAPP. Biochim. Biophys. Acta 1860, 1625–1638.

Sipe, J.D., Benson, M.D., Buxbaum, J.N., Ikeda, S.I., Merlini, G., Saraiva, M.J., Westermark, P., 2016. Amyloid fibril proteins and amyloidosis: chemical identification and clinical classification. Amyloid 23, 209–213.

So, M., Ishii, A., Hata, Y., Yagi, H., Naiki, H., Goto, Y., 2015. Supersaturation-limited and unlimited phase spaces compete to produce maximal amyloid fibrillation near the critical micelle concentration of sodium dodecyl sulfate. Langmuir 31, 9973–9982.

So, M., Hall, D., Goto, Y., 2016. Revisiting supersaturation as a factor determining amyloid fibrillation. Curr. Opin. Struct. Biol. 36, 32–39.

Tanner, J.E., 1970. Use of the stimulated echo in NMR diffusion studies. J. Chem. Phys. 52, 2523–2526.

Terakawa, M.S., Lee, Y.-H., Kinoshita, M., Lin, Y., Sugiki, T., Fukui, N., Ikenoue, T., Kawata, Y., Goto, Y., 2018. Membrane-induced initial structure of α-synuclein control its amyloidogenesis on model membranes. Biochim. Biophys. Acta 1860, 757–766.

Theillet, F.-X., Binolfi, A., Bekei, B., Martorana, A., Rose, H.M., Stuiver, M., Verzini, S., Lorenz, D., van Rossum, M., Goldfarb, D., et al., 2016. Structural disorder of monomeric α-synuclein persists in mammalian cells. Nature 530, 45.

Ugalde, C.L., Lawson, V.A., Finkelstein, D.I., Hill, A.F., 2019. The role of lipids in α-synuclein misfolding and neurotoxicity. J. Biol. Chem. 294, 9016–9028.

Umemoto, A., Yagi, H., So, M., Goto, Y., 2014. High-throughput analysis of the ultrasonication-forced amyloid fibrillation reveals the mechanism underlying the large fluctuation in the lag time. J. Biol. Chem. 289, 27290–27299.

Uversky, V.N., Lee, H.-J., Li, J., Fink, A.L., Lee, S.-J., 2001a. Stabilization of partially folded conformation during α-synuclein oligomerization in both purified and cytosolic preparations. J. Biol. Chem. 276, 43495–43498.

Uversky, V.N., Li, J., Fink, A.L., 2001b. Evidence for a partially folded intermediate in α-synuclein fibril formation. J. Biol. Chem. 276, 10737–10744.

Uversky, V.N., Li, J., Fink, A.L., 2001c. Metal-triggered structural transformations, aggregation, and fibrillation of human α-synuclein: a possible molecular link between Parkinson's disease and heavy metal exposure. J. Biol. Chem. 276, 44284–44296.

van der Goot, F.G., González-Mañas, J.M., Lakey, J.H., Pattus, F., 1991. A 'molten-globule' membrane-insertion intermediate of the pore-forming domain of colicin A. Nature 354, 408–410.

Voet, D., Voet, J.G., 1995. _Biochemistry_ Edn 2. J. Wiley & Sons, New York.

Weisemann, R., Rüterjans, H., Bermel, W., 1993. 3D Triple-resonance NMR techniques for the sequential assignment of NH and 15N resonances in 15N- and 13C-labelled proteins. J. Biomol. NMR 3, 113–120.

Wetzel, R., 2006. Kinetics and thermodynamics of amyloid fibril assembly. Acc. Chem. Res. 39, 671–679.

Yagi, H., Kusaka, E., Hongo, K., Mizobata, T., Kawata, Y., 2005. Amyloid fibril formation of α-synuclein is accelerated by preformed amyloid seeds of other proteins: implication for the mechanism of transmissible conformational diseases. J. Biol. Chem. 280, 38609–38616.

Yagi, H., Takeuchi, H., Ogawa, S., Ito, N., Sakane, I., Hongo, K., Mizobata, T., Goto, Y., Kawata, Y., 2010. Isolation of short peptide fragments from α-synuclein fibril core identifies a residue important for fibril nucleation: a possible implication for diagnostic applications. Biochim. Biophys. Acta 1804, 2077–2087.

Yagi, H., Abe, Y., Takayanagi, N., Goto, Y., 2014. Elongation of amyloid fibrils through lateral binding of monomers revealed by total internal reflection fluorescence microscopy. Biochim. Biophys. Acta 1844, 1881–1888.

Yagi, H., Mizuno, A., So, M., Hirano, M., Adachi, M., Akazawa-Ogawa, Y., Hagihara, Y., Ikenoue, T., Lee, Y.-H., Kawata, Y., et al., 2015. Ultrasonication-dependent formation and degradation of α-synuclein amyloid fibrils. Biochim. Biophys. Acta 1854, 209–217.

Yamaguchi, K-i, Naiki, H., Goto, Y., 2006. Mechanism by which the amyloid-like fibrils of a β₂-microglobulin fragment are induced by fluorine-substituted alcohols. J. Mol. Biol. 363, 279–288.

Yoshimura, Y., Lin, Y., Yagi, H., Lee, Y.-H., Kitayama, H., Sakurai, K., So, M., Ogi, H., Naiki, H., Goto, Y., 2012. Distinguishing crystal-like amyloid fibrils and glass-like amorphous aggregates from their kinetics of formation. Proc. Natl. Acad. Sci. U.S.A. 109, 14446–14451.

Žerovnik, E., Stoka, V., Mirtič, A., Gunčar, G., Grdadolnik, J., Staniforth, R.A., Turk, D., Turk, V., 2011. Mechanisms of amyloid fibril formation – focus on domain-swapping. FEBS J. 278, 2263–2282.